

Impact of a Fram Strait cyclone on ice edge, drift, divergence, and concentration: Possibilities and limits of an observational analysis

Burghard Brümmer,¹ David Schröder,² Gerd Müller,¹ Gunnar Spreen,³
Annika Jahnke-Bornemann,¹ and Jouko Launiainen⁴

Received 7 February 2007; revised 6 August 2008; accepted 28 August 2008; published 6 December 2008.

[1] This study aims at the determination of a Fram Strait cyclone track and of the cyclone's impact on ice edge, drift, divergence, and concentration. A 24 h period on 13–14 March 2002 framed by two RADARSAT images is analyzed. Data are included from autonomous ice buoys, a research vessel, Special Sensor Microwave Imager (SSM/I) and QuikSCAT satellite, and the operational European Centre for Medium-Range Weather Forecasts (ECMWF) model. During this 24 h period the cyclone moved northward along the western ice edge in the Fram Strait, crossed the northern ice edge, made a left-turn loop with 150 km diameter over the sea ice, and returned to the northern ice edge. The ECMWF analysis places the cyclone track 100 km too far west over the sea ice, a deviation which is too large for representative sea ice simulations. On the east side of the northward moving cyclone, the ice edge was pushed northward by 55 km because of strong winds. On the rear side, the ice edge advanced toward the open water but by a smaller distance because of weaker winds there. The ice drift pattern as calculated from the ice buoys and the two RADARSAT images is cyclonically curved around the center of the cyclone loop. Ice drift divergence shows a spatial pattern with divergence in the loop center and a zone of convergence around. Ice concentration changes as retrieved from SSM/I data follow the divergence pattern such that sea ice concentration increased in areas of divergence and decreased in areas of convergence.

Citation: Brümmer, B., D. Schröder, G. Müller, G. Spreen, A. Jahnke-Bornemann, and J. Launiainen (2008), Impact of a Fram Strait cyclone on ice edge, drift, divergence, and concentration: Possibilities and limits of an observational analysis, *J. Geophys. Res.*, *113*, C12003, doi:10.1029/2007JC004149.

1. Introduction

[2] Approximately 3000 km³ of sea ice drift from the Arctic Ocean through the Fram Strait into the North Atlantic Ocean per year. The amplitude of the interannual variability is about 50% of the mean value. This estimate is based on satellite data, moored upward looking sonars, and model simulations [e.g., Kwok *et al.*, 2004; Vinje and Finnekåsa, 1986; Hilmer *et al.*, 1998]. The variability of Fram Strait sea ice export is caused to a large extent by the variability of large-scale atmospheric circulation patterns [e.g., Vinje, 2001; Proshutinsky and Johnson, 1997; Deser *et al.*, 2000; Cavalieri, 2002], but also individual weather systems such as cyclones have a significant influence on the sea ice export.

[3] In a statistical study Affeld [2003] analyzes the relation between Fram Strait cyclones and ice export. He finds

that cyclones move predominantly with a south to north component through the Fram Strait. The cyclone impact on sea ice depends on the location of the cyclone track within the Fram Strait. The more easterly the track is located the larger is the ice export. This result is supported by numerical model experiments by Schröder [2005]. He simulates the impact of a prescribed cyclone which moves along various tracks through the Fram Strait. Schröder finds that a small shift of the cyclone track by only 100 km can already change the sign of the time-integrated effect of a cyclone event on Fram Strait ice export. Haapala *et al.* [2005] also performed idealized numerical experiments in which a cyclone moves over a closed homogeneous sea ice field. They obtain systematic reductions of sea ice concentration in the wake of the cyclone, but they mention that insufficient observations are available to validate the model results.

[4] Only very few observations of Fram Strait cyclones exist in the literature [Rasmussen *et al.*, 1997; Brümmer and Hoeber, 1999; Brümmer *et al.*, 2003; Brümmer *et al.*, 2005a]. These studies concentrate either on the atmospheric conditions or they are restricted by the availability of in situ measurements. This paper is meant as a contribution to improve the poor observational database on Fram Strait cyclones and their impact on the sea ice. In order to study

¹Meteorological Institute, University of Hamburg, Hamburg, Germany.

²Department of Environmental Meteorology, University of Trier, Trier, Germany.

³Institute of Oceanography, University of Hamburg, Hamburg, Germany.

⁴Finnish Institute of Marine Research, Helsinki, Finland.

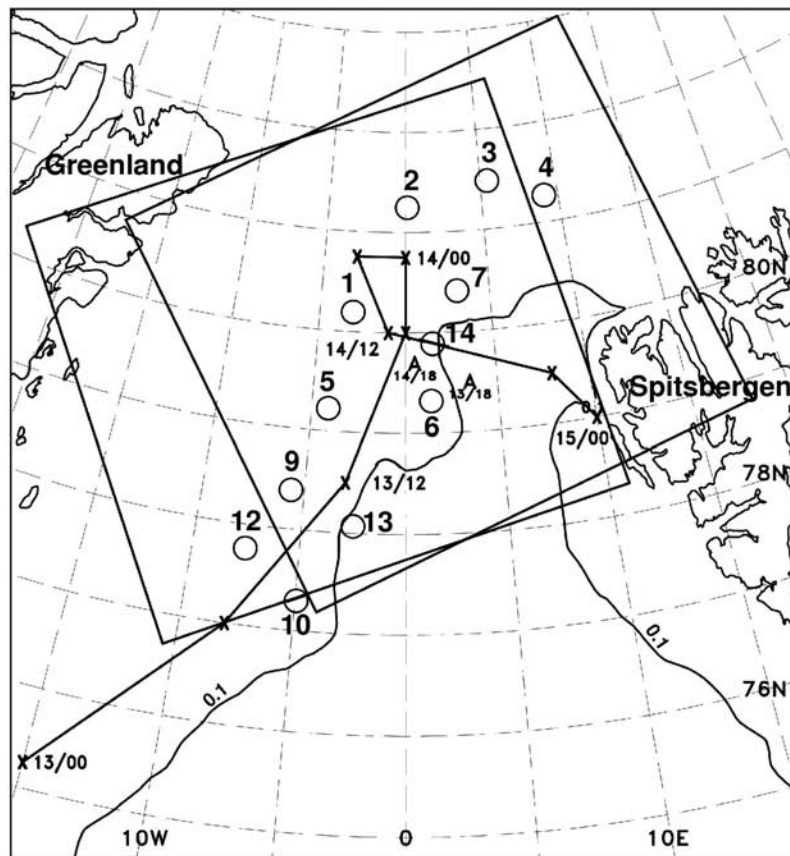


Figure 1. Research region in the Fram Strait. Large squares mark areas covered by two RADARSAT images on 13 March 2002 at 1649 UTC and 14 March at 1620 UTC. Circles give positions of 12 ARGOS ice buoys together with buoy number. “A” marks the position of R/V *Aranda* on 13 March at 1800 UTC and 14 March at 1800 UTC. Crosses connected by straight lines mark 6-hourly cyclone positions according to European Centre for Medium-Range Weather Forecasts (ECMWF) analyses between 13 March at 0000 UTC and 15 March at 0000 UTC. Solid line is 10% ice concentration from Special Sensor Microwave Imager (SSM/I) for 14 March.

the influence of a cyclone on sea ice, accurate knowledge is required of both the atmospheric forcing and the changes in sea ice distribution. *Haapala et al.* [2005] hint at the importance of accurate atmospheric forcing data for the validation of sea ice model results. Evaluations by *Curry et al.* [2002] reveal that there are still many problems regarding the accuracy of operational weather analyses in the Arctic and that the atmospheric forcing fields cannot be termed as sufficiently accurate.

[5] In this paper, an observational case study of a Fram Strait cyclone and its impact on ice edge, drift, divergence and concentration is presented. The cyclone event occurred in March 2002 during the Fram Strait cyclone expedition FRAMZY [Brümmer *et al.*, 2005b]. The aims of this paper are the following: (1) to determine the cyclone track as accurate as possible from the available observations and to compare the result to the operational European Centre of Medium-Range Weather Forecast (ECMWF) model analyses which are often used as atmospheric forcing in sea ice models and (2) to determine the temporal and spatial changes of the sea ice edge, drift, divergence, and concentration and to relate them to the cyclone track.

[6] For this study we combined all available atmospheric and sea ice data. This includes data from various satellites as well as in situ data from a research vessel and from drifting buoys. Despite the availability of these various data sets the combined data are still limited in space and time, limiting the extent of our analysis, and thus understanding of cyclone impacts on sea ice.

[7] The paper is organized as follows. The data compiled for this study are described in section 2. The atmospheric conditions during the cyclone event as analyzed from the observations and by the ECMWF model are presented in section 3. In section 4 the temporal and spatial changes of ice edge, drift, divergence and concentration in relation to the cyclone track are elaborated. Summary and conclusions are given in section 5.

2. Data Used in This Study

[8] For the cyclone event on 13–14 March 2002 we apply and compare information on the atmospheric forcing from the operational analyses of the ECMWF, from in situ measurements made by the Finnish research vessel (R/V) *Aranda* and by a fleet of 12 ARGOS ice buoys, and from

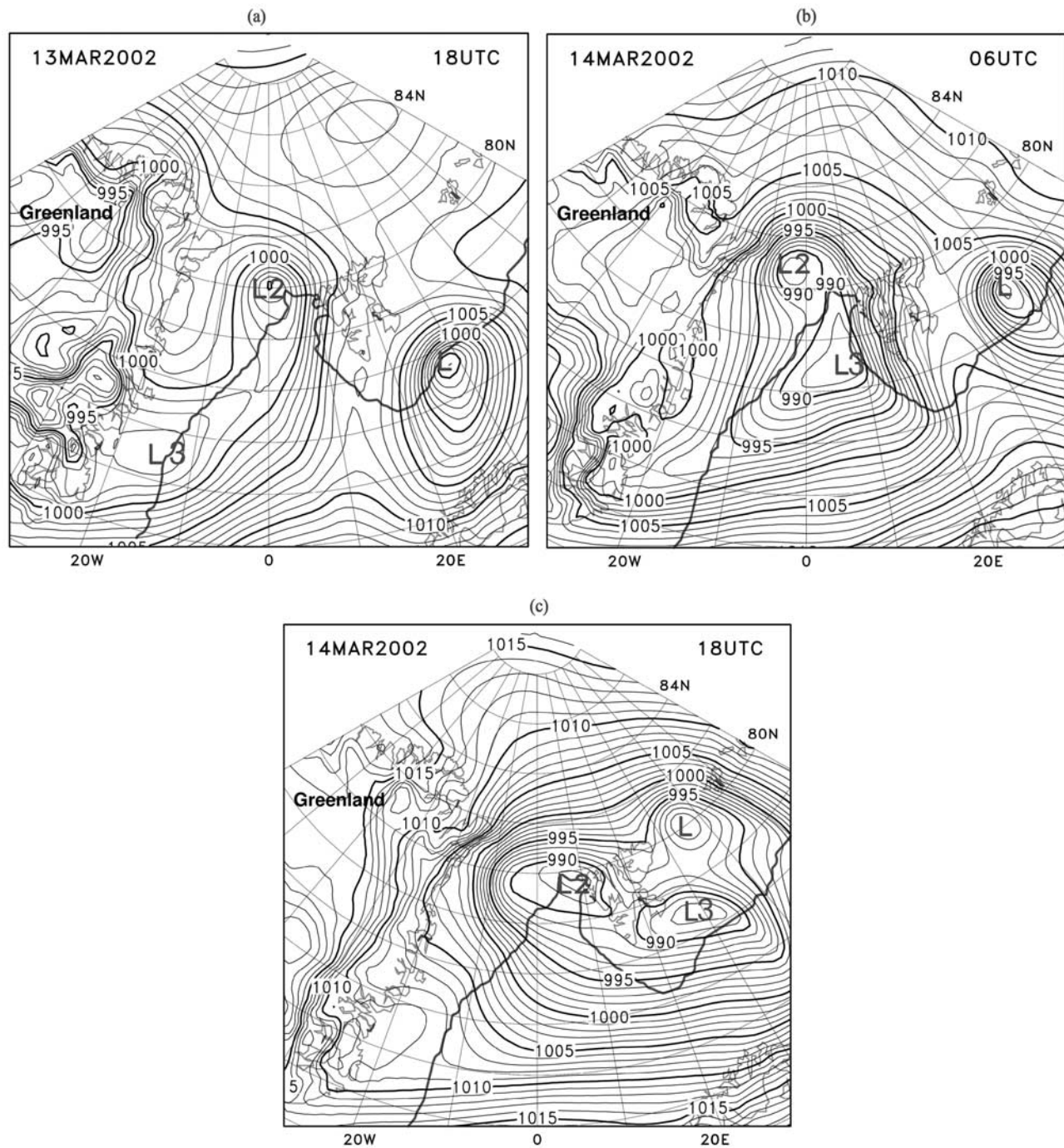


Figure 2. (a) Sea level pressure field as analyzed by ECMWF on 13 March at 1800 UTC. Thick line marks ice edge in ECMWF analysis. (b) As in Figure 2a but for 14 March at 0600 UTC. (c) As in Figure 2a but for 14 March at 1800 UTC.

Radar scatterometer wind measurements on the QuikSCAT satellite. Information on the sea ice conditions are taken also from the 12 ARGOS buoys, from two images of the RADARSAT satellite and from the SSM/I (Special Sensor Microwave Imager) sensor on the DMSP (Defense Meteorological Satellite Program) satellites. The geographical site of research is shown in Figure 1 together with the locations of the ARGOS buoys, R/V *Aranda*, the RADARSAT images and the average ice edge as derived from the

SSM/I. ECMWF and SSM/I data cover the whole area of Figure 1.

2.1. ECMWF Analyses

[9] ECMWF weather analyses are produced operationally every 6 h. The model-based analyses have a horizontal resolution of 0.5° in both latitude and longitude. Here, we use the sea level pressure (SLP) analyses. They give an overview of the large-scale synoptic situation during the

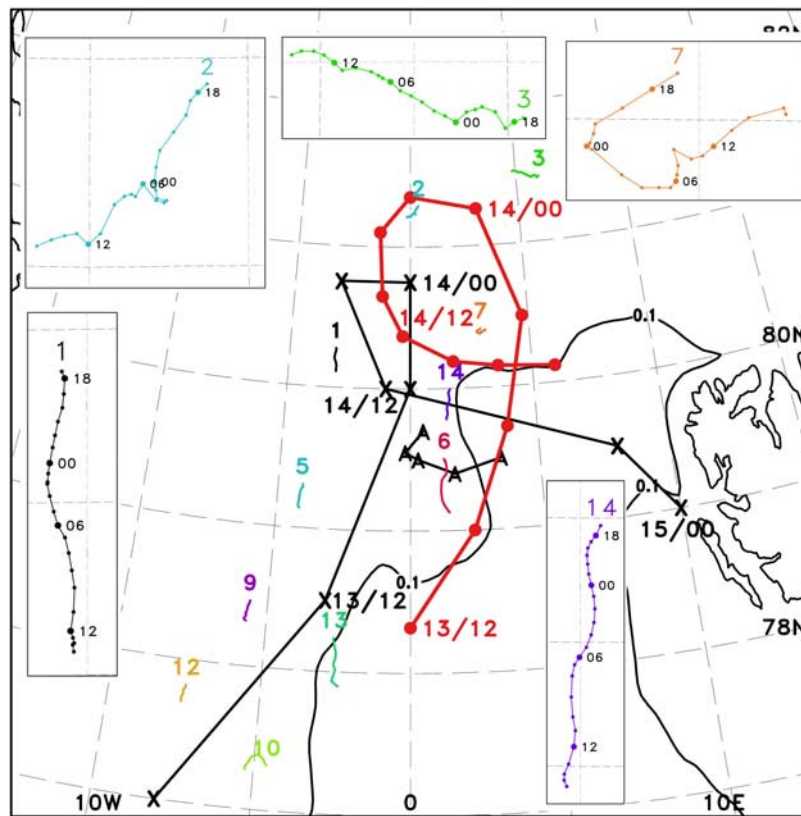


Figure 3. L2 cyclone track as analyzed by ECMWF (crosses mark 6-hourly cyclone positions) between 13 March at 0600 UTC and 14 March at 1800 UTC and as observed (dots mark 3-hourly positions) between 13 March at 1800 UTC and 14 March at 1800 UTC. Trajectories of ARGOS ice buoys (hourly positions) hold for the period 13 March at 1700 UTC to 14 March at 1700 UTC. Buoy trajectories in the vicinity of cyclone track are enlarged. “A” marks 6-hourly R/V *Aranda* position between 13 March at 1800 UTC and 14 March at 1800 UTC. Full line is 10% ice concentration from SSM/I for 14 March.

cyclone event. The cyclone track as analyzed by ECMWF is also displayed in Figure 1. The accuracy of the ECMWF analysis is tested by comparison with the in situ data of R/V *Aranda* and the ARGOS buoys in section 3.

[10] Sea ice concentration is a fixed lower boundary condition in ECMWF. Ice concentration is based on the corresponding daily NCEP (National Center for Environmental Prediction) product as described by Grumbine [1996]. The primary source of information is 19 GHz and 37 GHz SSM/I brightness temperatures from which sea ice concentrations are calculated using the algorithm described by Cavalieri *et al.* [1991]. To reduce weather contamination of the microwave signals a weather filter proposed by Gloersen and Cavalieri [1986] is applied. The NCEP sea ice concentration is transformed to the ECMWF grid. After transformation and interpolation, quality checks are applied in ECMWF with the result that, among others, sea ice concentration below 20% is set to 0%.

2.2. ARGOS Ice Buoys

[11] Two types of ice buoys were used (manufacturer: Metocean, Dartmouth, Canada): CALIB ice buoys and ice beacon buoys. CALIB buoys measure position, air pressure and air temperature. Ice beacon buoys have the same instrumentation and additional sensors for moisture, wind speed and wind direction. Wind is measured at a 3 m high

mast. At the beginning of the FRAMZY 2002 expedition, on 27 February 2002, 12 CALIB buoys were deployed in a regular 300 km (E–W) times 200 km (N–S) array centered at 81.5°N, 3°E. They were dropped from a transport aircraft and descended on parachutes. The array deformed in the course of the time because of differential ice drift. During the first two weeks of the expedition two CALIB buoys were lost at the ice edge so that only 10 of them are available for this study. Two ice beacon buoys (buoy numbers B13 and B14 in Figure 1) were deployed from R/V *Aranda* on 8 and 11 March. All buoys were equipped with the ARGOS system and data were transmitted at approximately hourly time intervals. Ice drift is calculated from the hourly buoy positions with an accuracy of 0.06 m s⁻¹ for both components (H. Hoeber, personal communication, 2000).

2.3. Research Vessel *Aranda*

[12] Between 1 and 25 March 2002, the Finnish R/V *Aranda* operated in the marginal ice zone in the northern part of the Fram Strait. During the cyclone event studied here, R/V *Aranda* steamed westward along 79.5°N from 4 to 0°E and later remained near 0°E (see Figure 4). We use measurements of air pressure, temperature, wind speed and direction taken at ship’s level at 10 min intervals. These data give valuable information on the temporal development of

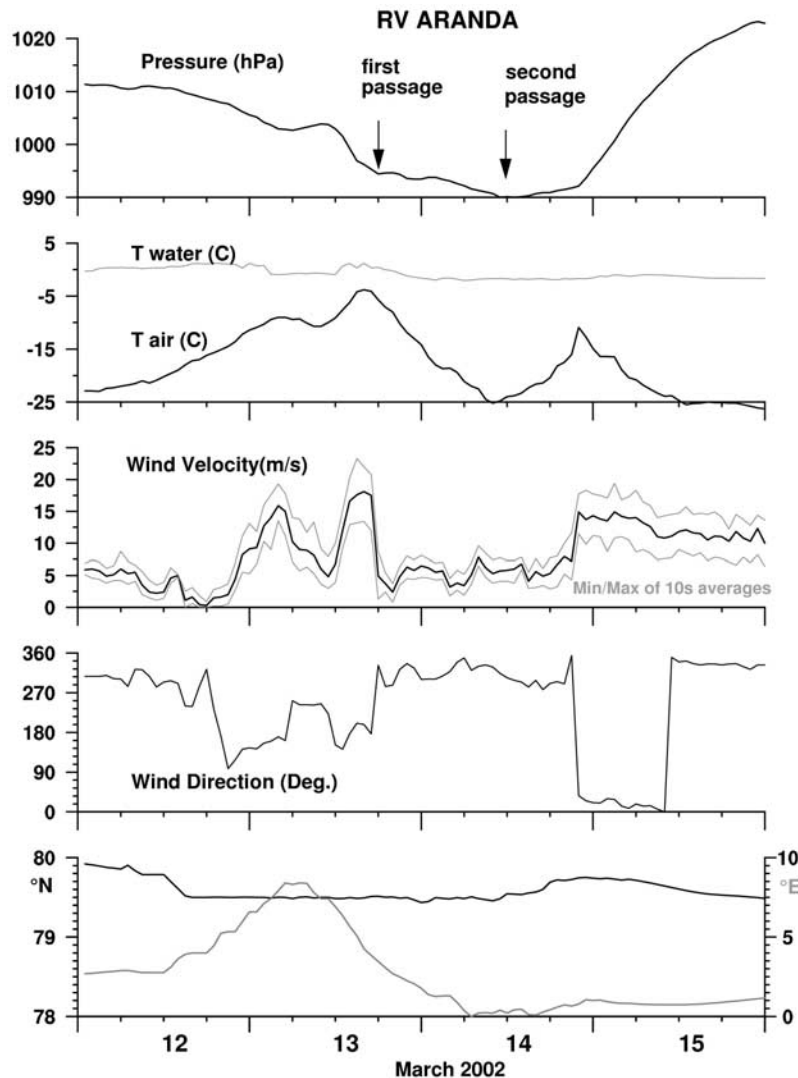


Figure 4. Time series of sea level pressure, air and water temperature, and wind speed and wind direction measured at R/V *Aranda*. The respective latitude and longitude positions are given in the fifth panel. Arrows mark the first passage of L2 west of R/V *Aranda* and the second passage north of R/V *Aranda*.

the atmospheric forcing at a “fixed” place during the cyclone passage.

2.4. RADARSAT Images

[13] Two successive wide mode RADARSAT images, valid for 13 March 2002 at 1649 UTC and for 14 March at 1620 UTC, are used in this study. They cover to a large extent the same area of the Fram Strait (see Figure 1). Each RADARSAT image is approximately 500 km times 450 km large with a grid resolution of 100 m times 100 m. The high spatial resolution allows the identification of marked structures in the ice field and their redetection in the following image. On the basis of the position differences of such marked structures between the two images, the ice drift was manually determined for about 90 locations. The method of ice drift determination from RADARSAT images has been applied by, e.g., Kwok [1998], Kwok *et al.* [2003], and Lindsay and Stern [2003]. The 90 drift vectors (with distances on the order of 30 km from each other) are

interpolated to a regular 30 km grid by objective analysis [Cressman, 1959]. Shear and divergence of the ice drift are then calculated for each grid point. The Cressman interpolation does not apply any preassumption about the divergence of the flow field.

2.5. SSM/I Satellite Data

[14] For the larger-scale view on the sea ice conditions SSM/I sea ice concentrations are used. SSM/I is a conically scanning radiometer with seven channels measuring at four frequencies (19, 22, 37, and 85 GHz). With a swath width of 1400 km SSM/I offers daily complete data coverage of the polar region. SSM/I images of the study region are not equally distributed over the day and cover for our study dates 13 and 14 March 2002 only the period from about 1200 to 1900 UTC. Here we use both daily means from all overpasses as well as data from two individual overpasses (swath data) at around 1600 UTC to keep the time differ-

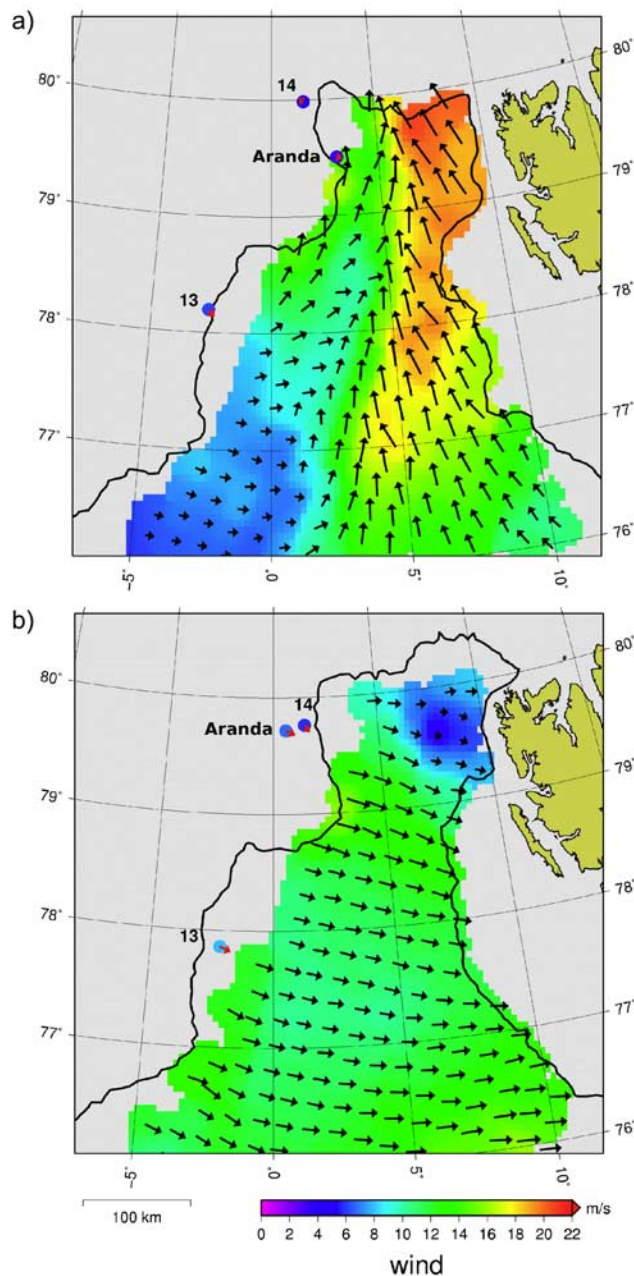


Figure 5. Wind fields over the open Fram Strait as retrieved from QuikSCAT on (a) 13 March 2002 at 1858 UTC and on (b) 14 March at 1832 UTC. In addition, the simultaneous wind measurements at buoys B13 and B14 and at R/V *Aranda* are presented as well as the SSM/I ice edge.

ence to the acquisition of the RADARSAT images as short as possible.

[15] The sea ice concentrations were calculated with the Arctic Radiation and Turbulence Interaction Study (ARTIST) Sea Ice (ASI) algorithm, which is based on that of Svendsen *et al.* [1987] and is described by Kaleschke *et al.* [2001] for SSM/I data as used here. The quality of the ASI algorithm was evaluated in several studies [e.g., Kern *et al.*, 2003, Andersen *et al.*, 2007, Spreen *et al.*, 2008]. The ASI algorithm uses the brightness temperature difference at

85 GHz between vertical (V) and horizontal (H) polarization, (T85V-T85H), to calculate sea ice concentrations. A time-invariant standard polar atmosphere is used to model the atmospheric influence on the brightness temperature difference and is a function of ice concentration. Two tie points which represent 100% ice cover ($P_{100} = 7.5$ K) and open water ($P_{00} = 47.0$ K) are needed. We use the ones found by Kaleschke *et al.* [2001] by comparison to aircraft NASA-Team ice concentrations. The lower frequency channels 19, 22, and 37 GHz of the SSM/I radiometer, which are less influenced by the atmosphere, and additionally NASA-Team ice concentrations [Cavalieri *et al.*, 1991; Comiso *et al.*, 1997] are used to eliminate spurious ice in the open ocean.

[16] With 16 km times 14 km footprint size 85 GHz channels offer the instruments highest spatial resolution, but the atmospheric influence is larger at this frequency as compared to the lower frequencies 19 and 37 GHz. Therefore, for comparison, we also use sea ice concentration derived from the Bootstrap algorithm [Comiso *et al.*, 1997], which utilizes these lower frequencies.

2.6. QuikSCAT Satellite Data

[17] For information on the low-level wind over the ice-free part of the Fram Strait we use the Ku-band (13.4 GHz) scatterometer SeaWinds onboard the QuikSCAT satellite (as it is the only instrument onboard we hereafter refer to it as QuikSCAT). QuikSCAT is capable of measuring daily near-surface winds over 90% of the world's ocean. Wind speed is retrieved with an accuracy better than 2 m/s for speeds between 3 and 20 m/s and with 10% relative accuracy for speeds between 20 and 30 m/s. The wind direction is retrieved with an accuracy of 20°. In this study we use the 25 km resolution Level 2B QuikSCAT swath data as distributed by the Physical Oceanography Distributed Active Archive Center (PO.DAAC) at the NASA Jet Propulsion Laboratory, Pasadena, CA (<http://podaac.jpl.nasa.gov>). The adopted reference height for the QuikSCAT wind is 10 m.

3. Atmospheric Conditions During the Cyclone Event of 13–14 March 2002

[18] The cyclone studied here was the second within a series of three cyclones which moved through the Fram Strait during the period 12–15 March. The second cyclone, called L2 in Brümmer *et al.* [2005a] and also hereafter, was present in the Fram Strait at and between the times of the two RADARSAT images. Figure 2 shows the large-scale SLP distribution as analyzed by ECMWF for three times: 13 March at 1800 UTC and 14 March at 0600 UTC and at 1800 UTC. The first and last SLP analyses are a little more than one hour later than the times of the RADARSAT images. Cyclone L2 moved from SW to NE near the ice edge, then moved further northward over the sea ice, then looped westward, and then finally left the Fram Strait in an eastward direction. The core pressure of L2 decreased until about 14 March at 1200 UTC then increased thereafter.

[19] The track of L2 as analyzed by ECMWF during its entire lifetime is presented in Figure 3 together with the drift trajectories of the ARGOS ice buoys. According to ECMWF, L2 moved directly through the buoy array.

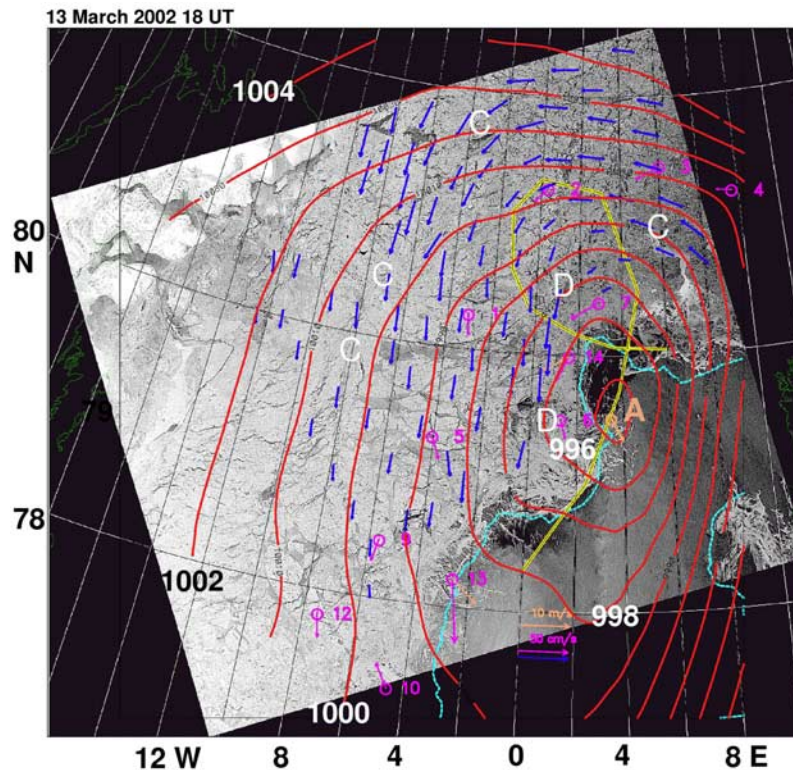


Figure 6. RADARSAT image taken on 13 March 2002 at 1649 UTC and superimposed sea level pressure field for 1800 UTC. Blue arrows are mean (24 h time interval) ice drift derived from this RADARSAT image and that in Figure 7. Pink arrows are actual (1 h time interval) ice drift from ARGOS buoys (circles). Orange arrows give wind speed at buoys B13 and B14 and R/V *Aranda* (indicated by “A”). Light blue line marks SSM/I ice edge for this day. The cyclone track (from Figure 3) is marked in yellow. “C” and “D” mark areas from maximum ice drift convergence and divergence (from Figure 10).

However, buoys B13, B6, and B14 on the eastside of the array show a southward ice drift over this time. This implies that L2 must have moved east of the buoy array toward N, where exactly is not known. The trajectories of B7 and B2 indicate that L2, on its way over the sea ice, must have passed B7 on the eastside and must have encircled B2.

[20] The measurements at R/V *Aranda* in Figure 4 show high air temperature and a sharp change from strong southerly to weaker northwesterly winds to have occurred on 13 March between 1700 and 1800 UTC when R/V *Aranda* was at a position of about 79.5°N, 4°E (shown in Figure 3). Thus, L2 must have passed closely west of R/V *Aranda* (between R/V *Aranda* and B6). The relative pressure minimum recorded at R/V *Aranda* during the passage of L2 is not very distinct because the whole L2 system deepened further. The second passage of L2 near R/V *Aranda* (after L2 circled round B2 and B7) is indicated by the absolute pressure minimum in Figure 4.

[21] In Figures 5a and 5b two wind fields are presented from the QuikSCAT overpasses on 13 March at 1858 UTC and on 14 March at 1832 UTC. The first wind field demonstrates that L2 did not move over the open water of the Fram Strait but west of it. On the basis of this observation and the observation in Figure 3, namely that L2 passed east of the buoy array, we conclude that L2 must have moved along the ice edge. Coupled atmosphere-sea ice model simulations of Dierer and Schluenzen [2005] and

Dierer *et al.* [2005] indicate that the ice edge zone is the preferred cyclone track in case of absence of other strong synoptic constraints. The second QuikSCAT wind field confirms that L2 (after its loop over the sea ice) moved north of 80°N and toward the east.

[22] The likely track of L2 as inferred from the data of R/V *Aranda*, the ARGOS buoys and the QuikSCAT wind is displayed in Figure 3. Compared to this, the L2 track in ECMWF is located about 100 km too far west (west of the ice edge) and does not extend so far north (about 80 km less). Considering the numerical experiments by Schröder [2005] with an idealized cyclone and the resulting sensitive dependence of Fram Strait ice export on the location of the cyclone track, the present ECMWF cyclone analysis is not accurate enough to use it as atmospheric forcing for an accurate cyclone impact simulation. The difference between the observed and ECMWF-analyzed cyclone track in this case underlines the statement made by Haapala *et al.* [2005] that there is still a long way to go for adequate forcing fields in the polar region.

[23] The measurements at R/V *Aranda* document a large temperature contrast of almost 20 K between the warm and cold side of L2 and high wind speeds in connection with L2 with maximum values of 18 m s⁻¹ for a 1 h average and 23 m s⁻¹ for a 10 min average. Similarly high amplitudes of temperature contrast and wind were reported by Brümmér and Hoeber [1999] for another Fram Strait cyclone case.

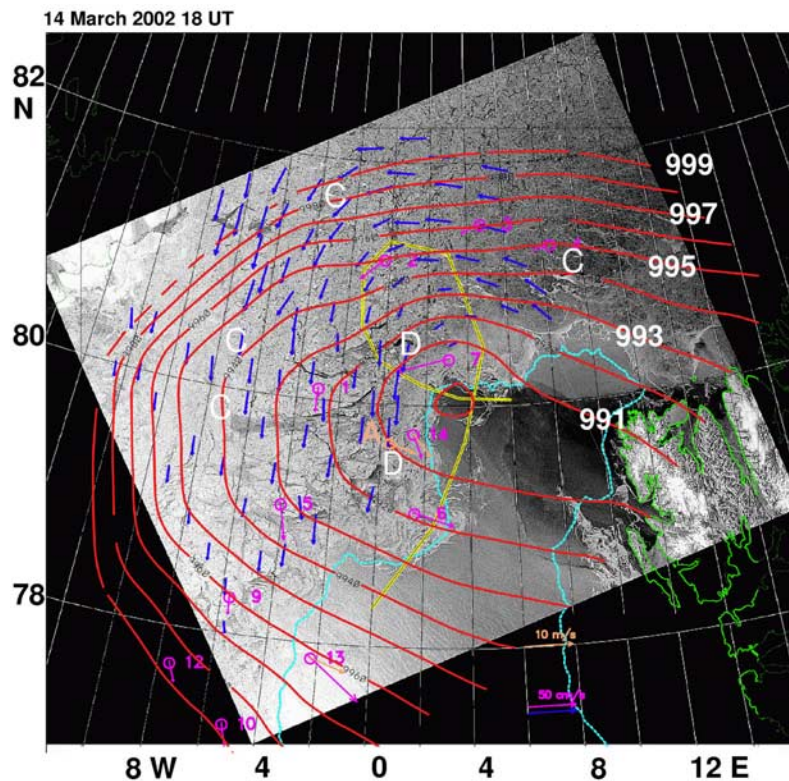


Figure 7. As Figure 6 but for RADARSAT image on 14 March 2002 at 1620 UTC and for SLP field at 1800 UTC.

These studies demonstrate the potential of Fram Strait cyclones to strongly impact the sea ice and underline the necessity of their accurate analysis in order to be able to simulate sea ice in this region accurately.

4. Sea Ice Conditions During the Cyclone Event

[24] In sections 4.1 and 4.2, we investigate the cyclone's impact on ice edge, drift, divergence, and concentration. As mentioned above, the investigation is based on RADARSAT images, SSM/I data, and ARGOS ice buoys.

4.1. Impact on Ice Edge

[25] The two RADARSAT images are displayed in Figures 6 and 7. They represent the sea ice conditions on 13 March at 1649 UTC and 14 March at 1620 UTC; approximately at the beginning and end of the cyclone loop over the sea ice (Figure 3). Superimposed on each RADARSAT image is the SLP distribution for 1800 UTC. It is composed from the SLP data of the ARGOS buoys in the center of the images and from SLP readings of the ECMWF analysis in the surrounding at distances of at least 50 km from the buoys.

[26] As a result of the cyclone loop, there are sections along the ice edge which remained in the same airflow direction during the entire time interval between the two RADARSAT images. This is true for the northeast and southwest section of the Fram Strait ice edge but with opposite flow directions. In the northeast section around 80°N, 8°E continuous south-southeasterly on-ice airflow pushed the ice edge about 55 km northward within 24 h.

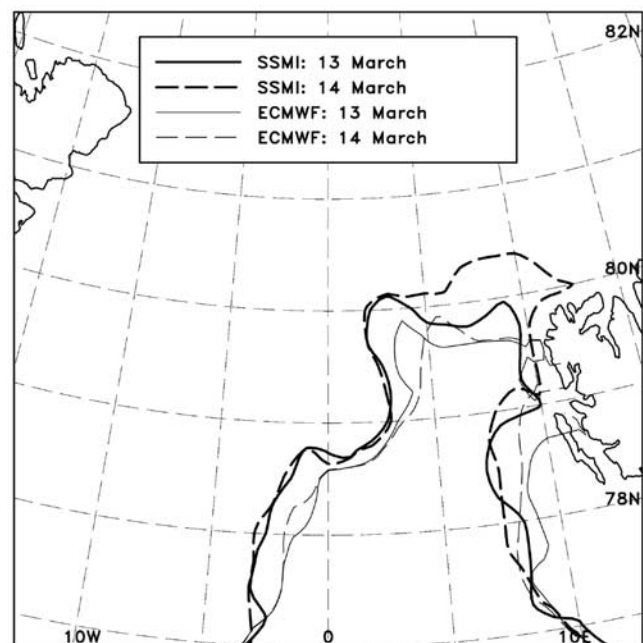


Figure 8. Ice edge (10% ice concentration) retrieved from SSM/I on 13 (thick solid line) and 14 (thick dashed line) March and given in ECMWF analysis on 13 (thin solid line) and 14 (thin dashed line) March 2002.

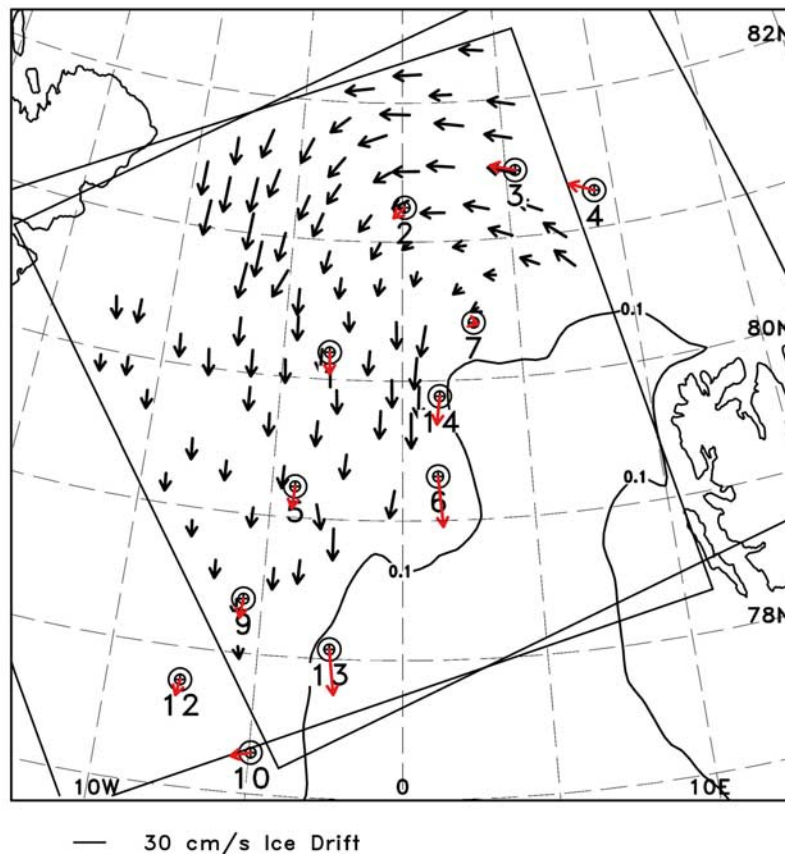


Figure 9. Mean ice drift (23.5 h: 13 March at 1649 UTC until 14 March at 1620 UTC) from RADARSAT images (black arrows) and 12 ARGOS ice buoys (red arrows). Solid line marks SSM/I ice edge on 14 March.

Here, the ice edge is rather sharp and compressed (high radar backscatter). In the southwest section around 78°–79°N, 2°W–2°E continuous off-ice airflow from westerly to northerly direction caused the sea ice to drift toward southeast. Here, the ice edge is diffuse with many ice filaments. In this region the ice edge did not progress much toward SE within 24 h because the winds southwest of the cyclone were much weaker than east of the center as indicated by the isobars in Figure 6.

[27] The ice edge as retrieved from SSM/I (10% ice concentration) is superimposed on the RADARSAT images in Figures 6 and 7 for comparison. The SSM/I ice edge (daily mean, ASI algorithm) approximates the RADARSAT ice edge in a smoothed manner because of the coarser resolution. However, there are deviations between the RADARSAT and SSM/I derived ice edges in the above mentioned two regions most heavily influenced by the cyclone passage (see Figure 7): (1) between 8° and 12°E and 80.5°N, the SSM/I ice edge is further south than the compact ice edge in the RADARSAT image, and (2) between 2° and 4°E and around 79°N the SSM/I ice edge is further west than the diffuse and filamentous ice edge in the RADARSAT image.

[28] In Figure 8 the SSM/I ice edge (daily mean) is compared with the ice edge used in the ECMWF analyses. Deviations of the ECMWF ice edge from the SSM/I ice edge are smaller than 25 km on the west side of the Fram

Strait. A significant deviation of about 60 km occurs north of 80°N and between 7° and 11°E on 14 March. The substantial northward movement of the ice edge from 13 to 14 March caused by the L2 passage is not present in the ECMWF data. It is unlikely that the rather small deviations at the western ice edge are the reason that the L2 cyclone track in the ECMWF analysis is located too far west. However, the too far south located ECMWF ice edge in the northern part of the Fram Strait on 14 March may be the reason that the ECMWF cyclone track did not extend so far north over the sea ice as observed.

4.2. Impact on Ice Drift, Divergence, and Concentration

[29] The mean ice drift as derived from the two RADARSAT images and from the 12 ARGOS buoys (for the same 24 h time interval) is shown in Figure 9. The ice drift from both methods agrees well. The drift field is cyclonically curved and reflects the mean atmospheric flow around the L2 cyclone. According to Figure 9 the smallest ice drift (nearly stagnation) occurs in the area near buoy B7. This is close to the center of the cyclone loop over the sea ice (see also Figure 3). The largest ice drift within the ice pack with values up to 0.32 m s^{-1} occurs in the northwest (81°–82°N, 5°–10°W) where the strongest SLP gradients are present according to the ECMWF analysis (Figure 2). The absolutely largest ice drift occurs at the western ice

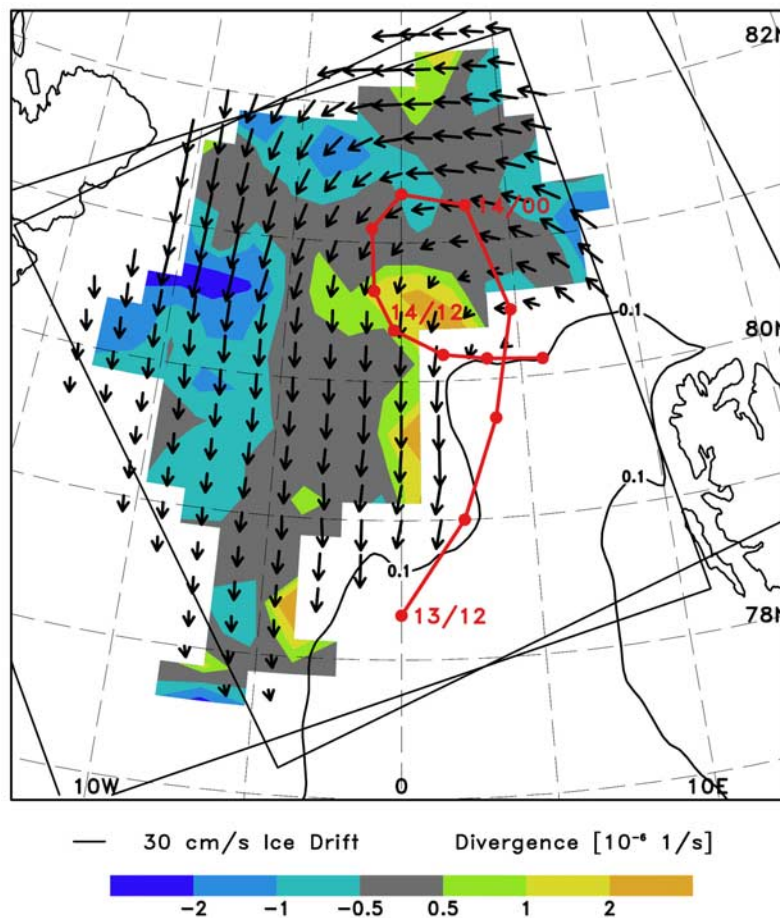


Figure 10. Ice drift interpolated on a regular grid and ice drift divergence (underlaid) calculated therefrom. The red line marks the observed L2 cyclone track. Thin line is SSM/I ice edge on 14 March.

edge of the Fram Strait (between buoys B14, B6, and B13) with values up to 0.45 m s^{-1} .

[30] To calculate the divergence, the observed ice drift was interpolated on a regular 30 km grid. The result is displayed in Figure 10. The divergence is spatially arranged in three zones. (1) Divergence is present within and close to the south and west of the cyclone loop center and along the western ice edge. (2) Adjacent to these areas follows a streak with predominantly neutral divergence. (3) Further outside (at distances of about 150 km from the cyclone loop center and from the western ice edge) follows a streak with ice drift convergence. Divergence within each of these three zones is not homogeneously distributed but speckled. This may be caused by the nonregularity of the observational data or may result from the fact that the sea ice is not a continuum but consists of ice floes of different sizes. The divergence on the floe scale is zero as, e.g., in the area between buoys B1 and B5 where many large floes are present.

[31] In order to validate the spatial distribution of divergence in Figure 10, ice drift divergence, $\nabla \vec{v}_{ice}$, was additionally calculated from the ARGOS ice buoy data according to

$$\nabla \vec{v}_{ice} = \frac{1}{A} \frac{dA}{dt},$$

where A is the area of a triangle or square formed by ARGOS buoys and t is time. Figure 11a represents the mean (24 h average) divergence for six different areas: A1–A6. In accordance with Figure 10, the divergence is also systematically distributed. Convergence occurs in the northern and southern part of the buoy array. Divergence is found between those two areas with maximum values in the region of buoy B14.

[32] The temporal variation of the divergence within and around the 24 h period framed by the times of the two RADARSAT images is presented in Figure 11b by means of the temporal development of A in the six areas. Divergence/convergence undergoes different temporal variations within the six areas. Short-term (1–3 h) variations of A can reflect uncertainties of the buoy positions. More interesting are the longer-term (>6 h) variations or trends. During the period between the two RADARSAT images, there are areas which continuously experience convergence (area A1) or divergence (A3 and A5), and there are other areas in which divergence changes with time according to their relative position to cyclone L2. When the area is located close to or closely west/southwest of the cyclone core, divergence is present. This is particularly obvious for area A4 during the period 1000–2400 UTC on 13 March, when L2 is east and later northeast of the area, and for area A2 between 0100 and 1800 UTC on 14 March, when L2 is in the area. Thus,

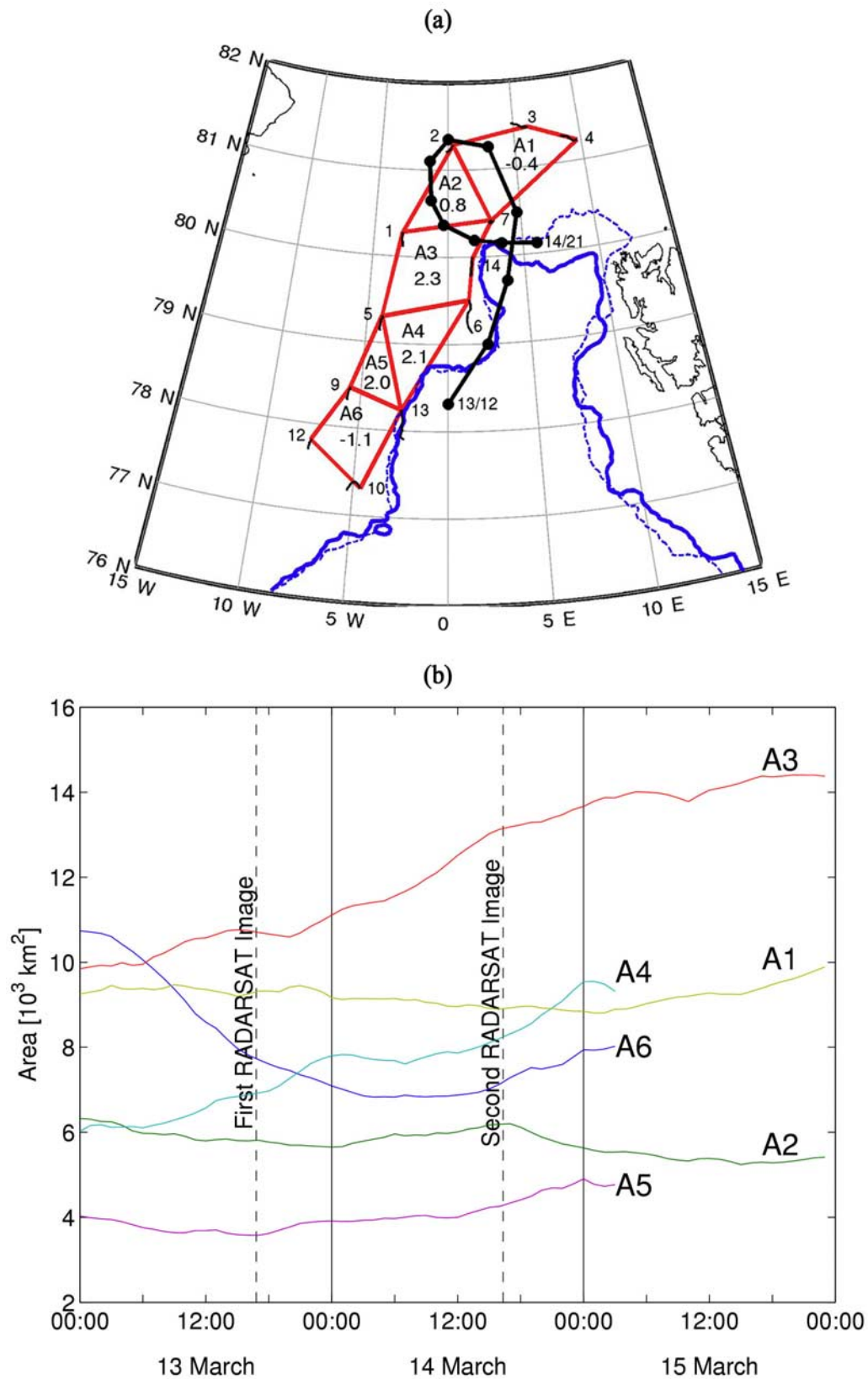


Figure 11. (a) Mean divergence (24 h average for time period between first and second RADARSAT image; units 10^{-6} s^{-1}) in six subareas A1–A6 formed by the ARGOS buoys from 13 to 15 March 2002. (b) Time variation of subareas A1–A6 in Figure 11a from 13 to 15 March 2002. Time series for A4–A6 end on 15 March at 0400 UTC because buoy B13 was lost at that time.

we conclude that the time variation of divergence/convergence within the various areas supports the systematic divergence pattern around the cyclone: divergence near the core and closely west and southwest of it, followed by a neutral zone around and then followed by a zone of convergence even further outside around the cyclone. We are aware that these findings still remain uncertain to some degree because of the coarse spatial buoy coverage and that further observations would be needed to confirm the spatial distribution of divergence/convergence around the cyclone center.

[33] Divergence or convergence of the ice drift should also influence the ice concentration in the respective region. We use ice concentrations derived by two different algorithms (ASI and Bootstrap) from SSM/I data for comparison (see section 2.5). The SSM/I ice concentration, n_{ice} , for the satellite overpass on 13 March at about 1600 UTC is shown in Figure 12a and the changes in ice concentration, Δn_{ice} , between the overpasses on 13 March at 1600 UTC and on 14 March at 1600 UTC for the two different algorithms are presented in Figures 12b and 12c, respectively. At the ice edge, Δn_{ice} , is negative in the northeast and positive in the southwest in accordance with the ice edge displacements measured by RADARSAT (compare Figures 6 and 7). In the center of the L2 cyclone loop an increase of ice concentration ($\Delta n_{ice} > 0$) and at the outer periphery of the loop a decrease of ice concentration ($\Delta n_{ice} < 0$) is calculated from the 85 GHz SSM/I derived ice concentration retrievals. Thus, ice concentration increased in areas of divergence and decreased in areas of convergence. If observations of both, Δn_{ice} and $\nabla \vec{v}_{ice}$, are correct, it must be concluded that other processes than ice drift divergence dominated the changes Δn_{ice} . Drift convergence occurred in areas that already had $n_{ice} > 95\%$, while drift divergence occurred in areas near the ice edge, where n_{ice} is smaller. The preexisting sea ice concentration clearly will have some bearing on how convergence/divergence will consequently impact the resulting sea ice concentration changes. We are aware that the magnitude of Δn_{ice} in the mentioned regions of divergence and convergence is small (close to the accuracy of the SSM/I ice concentration measurement which can be influenced by atmospheric water vapor and liquid water). If we use the 19/37 GHz channels of SSM/I which have a coarser resolution but are less weather contaminated, a similar pattern of Δn_{ice} is obtained as shown in Figure 12c. Unfortunately, there is a large gap in the time series of SSM/I images in the study region between the last image on 13 March at about 1900 UTC and the first image on 14 March at about 1200 UTC. This limits further insight into the temporal variation of n_{ice} and thus a better understanding of the processes involved.

[34] The changes in the two RADARSAT images in the regions of maximum divergence (marked by “D” in Figures 6 and 7) qualitatively suggest an increase of the “dark” areas with small radar backscatter, i.e., an increase of openings. However, a correct classification whether this is open water or new ice is not possible because of overlap in the radar backscatter distributions of these two surface types depending on the stage of the new-ice development, wind strength, and other variables [e.g., Kwok and Cunningham, 2002; Bogdanov et al., 2005].

[35] Finally, we note the strong increase of Δn_{ice} at the ice edge far in the southwest (around 77°N) of the Fram Strait (Figure 12). This is the effect of a third cyclone L3 which also moved northeastward, but along a more southern track than L2 (see Figures 2a–2c).

5. Summary and Conclusions

[36] An observational case study of a cyclone over the Fram Strait and of its impact on the sea ice edge, drift, divergence, and concentration is presented to supplement the insufficient number of well-documented observations which can be used as basis for model validation. The study is based on in situ data from autonomous ARGOS buoys and from a research vessel, on RADARSAT, SSM/I and QuikSCAT satellite observations, and on the operational model analyses of the ECMWF. A study of cyclone impact on sea ice requires both an analysis of the atmospheric forcing and an analysis of the impact on sea ice. Both aspects are covered in this paper.

[37] The cyclone L2 studied here moves along the western ice edge in the Fram Strait toward north and, later, crosses the northern ice edge. From there it moves about 150 km over the sea ice and, afterwards, returns on a looping-like track. The loop of cyclone L2 and thus its 24 h long residence within a 150 km times 150 km large area lead to a continuous south/southeasterly airflow in the northeast part of the Fram Strait and to an ice edge displacement of 55 km toward north. Simultaneously, a continuous, but weaker west/northwesterly airflow on the southwest side of the cyclone loop causes a small ice edge displacement toward the open ocean.

[38] The ECMWF analysis puts the northward track of cyclone L2 about 100 km too far in the west over the ARGOS buoy array and also the subsequent cyclone loop over the sea ice does not extend so far north as observed. The western ice edge in the ECMWF analysis is realistically located and cannot be the reason for the misplaced cyclone track. The shift of the northern ice edge toward north caused by the cyclone L2 is not accounted for in the ECMWF and may be the reason that L2 in the ECMWF analysis does not move so far northward over the ice. But also the determination of the real cyclone track from the observations is limited: the track of L2 along the ice edge could only be indirectly inferred because the ARGOS ice buoys only give information over the ice and the QuikSCAT winds only over the open ocean. Thus, a stripe along the ice edge without measurements remains. However, this uncertainty does not affect the clear falsification of the ECMWF cyclone track over the sea ice by the ARGOS buoys. Considering the model studies of Schröder [2005] on the sensitivity of the Fram Strait ice export on the location of the cyclone track relative to the ice edge, it can be concluded that the ECMWF sea level pressure analysis of the L2 cyclone track is not accurate enough to serve as atmospheric forcing in a sea ice model which aims at a realistic simulation Fram Strait ice export.

[39] The ice drift field derived over a 24 h interval from the two RADARSAT images and the ARGOS ice buoys is cyclonically arranged around the region of the cyclone loop. Minimum drift velocity occurs in the center of the loop. Ice drift divergence appears to be systematically distributed:

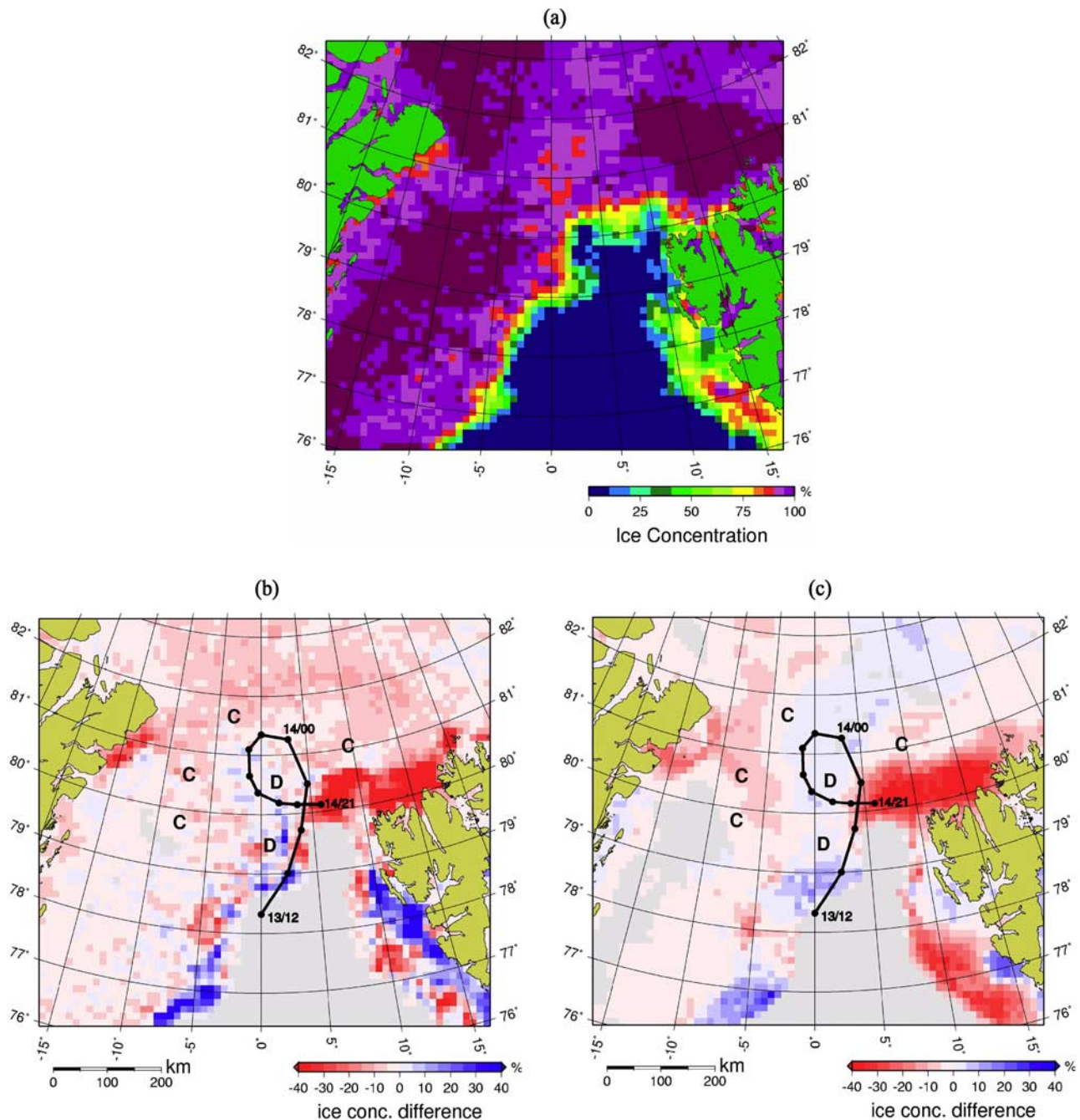


Figure 12. (a) SSM/I ice concentration on 13 March 2002 at 1600 UTC (85 GHz channel, Arctic Radiation and Turbulence Interaction Study (ARTIST) Sea Ice (ASI) algorithm). (b) Difference of SSM/I ice concentration on 14 March at 1600 UTC minus 13 March 2002 at 1600 UTC (85 GHz channel, ASI algorithm). Thick line is observed L2 cyclone track. “C” and “D” mark locations of maximum convergence and divergence (see Figure 10), respectively. (c) As Figure 12b but for 19/37 GHz channels, Bootstrap algorithm.

divergence in the center with some indication of a south-westward extension, a neutral divergence zone around it and convergence around the outer periphery.

[40] According to the ice concentration retrieved from SSM/I the pattern of ice concentration change with time resembles the ice drift divergence pattern, but in an opposite manner than expected: concentration increases where divergence is present and vice versa. However, divergence and

concentration increase occurred in or near the marginal ice zone, while convergence and concentration decrease occurred in areas that already had $n_{ice} > 95\%$. This implies that the preexisting sea ice concentration has some bearing on how convergence/divergence impact the resulting sea ice concentration changes. These observational findings require further investigation. It can be speculated that an increase of water vapor and cloud liquid water content in the atmo-

sphere between 13 and 14 March 2002 caused by the passing cyclone could be responsible for the positive SSM/I ice concentration difference in the center of the cyclone track. High water vapor and cloud liquid water values can lead to an overestimation of SSM/I derived ice concentrations even for the lower frequency channels [Maslanik, 1992]. Additionally leads which opened in the divergent zones may be quickly refrozen again under winter conditions and thus detected as ice covered by the SSM/I algorithms.

[41] In spite of the use of a wide range of data from various state-of-the-art observation sources, there still remain uncertainties caused by measurement deficiencies. The data coverage both in time and space is too coarse to determine the exact location of the cyclone track and the pressure field around it as well as the time and space variations of ice drift and concentration caused by the cyclone. To reach these goals adequately atmospheric and sea ice data with about 1 h time resolution and about 25 km space resolution would be necessary. ARGOS buoy and ship measurements have a fine temporal resolution (order 1 h), but large (order 100 km) spatial gaps, whereas SSM/I and particularly RADARSAT images have a fine spatial resolution (order 20 km and 100 m, respectively), but an unsatisfactory temporal resolution (order 1 day). Since these observational deficiencies/constraints will not improve in the foreseeable future, the possibilities of observational analyses of cyclone impact on sea ice will remain limited. Progress, and thus consolidation of the findings in this study, can be expected from the analysis of more cases and the use of numerical modeling closely connected to the observations.

[42] **Acknowledgments.** This study was funded by the German Science Foundation (DFG) within the Special Research Compound (SFB 512) entitled "Cyclones and the North Atlantic climate system." The QuikSCAT/SeaWinds wind vector data were obtained from the Physical Oceanography Distributed Active Archive Center (PO.DAAC) at the NASA Jet Propulsion Laboratory, Pasadena, California.

References

- Affeld, B. (2003), *Zyklonen in der Arktis und ihre Bedeutung für den Eisexport durch die Framstraße*, Ph.D. thesis, 130 pp., Dep. of Geosci., Univ. of Hamburg, Hamburg, Germany.
- Andersen, S., R. Tonboe, L. Kaleschke, G. Heygster, and L. T. Pedersen (2007), Intercomparison of passive microwave sea ice concentration retrievals over the high-concentration Arctic sea ice, *J. Geophys. Res.*, **112**, C08004, doi:10.1029/2006JC003543.
- Bogdanov, A., S. Sandven, O. Johannessen, V. Y. Alexandrov, and L. Bobylev (2005), Multisensor approach to automated classification of sea ice image data, *IEEE Trans. Geosci. Remote Sens.*, **43**(7), 1648–1664, doi:10.1109/TGRS.2005.846882.
- Brümmer, B., and H. Hoerber (1999), A mesoscale cyclone over the Fram Strait and its effects on sea ice, *J. Geophys. Res.*, **104**(D16), 19,085–19,098, doi:10.1029/1999JD900259.
- Brümmer, B., G. Müller, and H. Hoerber (2003), A Fram Strait cyclone: Properties and impact on ice drift as measured by aircraft and buoys, *J. Geophys. Res.*, **108**(D7), 4217, doi:10.1029/2002JD002638.
- Brümmer, B., G. Müller, and D. Schröder (2005a), In situ observations in cyclones over Fram Strait, *Meteorol. Z.*, **14**, 721–734, doi:10.1127/0941-2948/2005/0082.
- Brümmer, B., J. Launiainen, G. Müller, and D. Schröder (2005b), Field experiment FRAMZY 2002: Second experiment on cyclones over the Fram Strait and their impact on sea ice, Field report with examples of measurements, *Beitr. Zent. Meeres Klimaforsch., Reihe A*, **37**, 134 pp.
- Cavalieri, D. J. (2002), A link between Fram Strait sea ice export and atmospheric planetary wave phase, *Geophys. Res. Lett.*, **29**(12), 1614, doi:10.1029/2002GL014684.
- Cavalieri, D. J., J. P. Crawford, M. R. Drinkwater, D. T. Eppler, L. D. Farmer, R. R. Jentz, and C. C. Wackerman (1991), Aircraft active and passive microwave validation of sea ice concentration from the Defense Meteorological Satellite Program special sensor microwave imager, *J. Geophys. Res.*, **96**(C12), 21,989–22,008, doi:10.1029/91JC02335.
- Comiso, J. C., D. J. Cavalieri, C. L. Parkinson, and P. Gloersen (1997), Passive microwave algorithms for sea ice concentration: A comparison of two techniques, *Remote Sens. Environ.*, **60**(3), 357–384, doi:10.1016/S0034-4257(96)00220-9.
- Cressman, G. P. (1959), An operational objective analysis system, *Mon. Weather Rev.*, **87**, 367–374, doi:10.1175/1520-0493[1959]087<0367:AOOAS>2.0.CO;2.
- Curry, J. A., J. L. Schramm, A. Alam, R. Reeder, T. E. Arbetter, and P. Guest (2002), Evaluation of data sets used to force sea ice models in the Arctic Ocean, *J. Geophys. Res.*, **107**(C10), 8027, doi:10.1029/2000JC000466.
- Deser, C., J. E. Walsh, and M. S. Timlin (2000), Arctic sea ice variability in the context of recent atmospheric circulation trends, *J. Clim.*, **13**, 617–633, doi:10.1175/1520-0442[2000]013<0617:ASIVIT>2.0.CO;2.
- Dierer, S., and K. H. Schlunzen (2005), Influence parameters for a polar mesocyclone development, *Meteorol. Z.*, **14**, 781–792, doi:10.1127/0941-2948/2005/0077.
- Dierer, S., K. H. Schlunzen, G. Birnbaum, B. Brümmer, and G. Müller (2005), Atmosphere–sea ice interactions during a cyclone passage investigated by using model simulations and measurements, *Mon. Weather Rev.*, **133**, 3678–3692, doi:10.1175/MWR3076.1.
- Gloersen, P., and D. J. Cavalieri (1986), Reduction of weather effects in the calculation of sea ice concentration from microwave radiances, *J. Geophys. Res.*, **91**(C3), 3913–3919, doi:10.1029/JC091iC03p03913.
- Grumbine, R. W. (1996), Automated passive microwave sea ice concentration analysis at NCEP, *Tech. Note*, 120, 13 pp., Ocean Model. Branch, Natl. Cent. for Environ. Predict., Camp Springs, Md.
- Haapala, J., N. Lönnroth, and A. Stössel (2005), A numerical study of open water formation in sea ice, *J. Geophys. Res.*, **110**, C09011, doi:10.1029/2003JC002200.
- Hilmer, M., M. Harder, and P. Lemke (1998), Sea ice transport: A highly variable link between Arctic and North Atlantic, *Geophys. Res. Lett.*, **25**(17), 3359–3362, doi:10.1029/98GL52360.
- Kaleschke, L., C. Luepkes, T. Vihma, J. Haarpaintner, A. Bocher, J. Hartmann, and G. Heygster (2001), SSM/I sea ice remote sensing for mesoscale ocean-atmosphere interaction analysis, *Can. J. Rem. Sens.*, **27**(5), 526–537.
- Kern, S., L. Kaleschke, and D. A. Clausi (2003), A Comparison of two 85-GHz SSM/I ice concentration algorithms with AVHRR and ERS-2 SAR imagery, *IEEE Trans. Geosci. Remote Sens.*, **41**(10), 2294–2306, doi:10.1109/TGRS.2003.817181.
- Kwok, R. (1998), The RADARSAT geophysical processor system, in *Analysis of SAR Data of the Polar Oceans: Recent Advances*, edited by C. Tsatsoulis and R. Kwok, pp. 235–257, Springer, New York.
- Kwok, R., and G. F. Cunningham (2002), Seasonal ice area and volume production of the Arctic Ocean: November 1996 through April 1997, *J. Geophys. Res.*, **107**(C10), 8038, doi:10.1029/2000JC000469.
- Kwok, R., G. F. Cunningham, and W. D. Hibler III (2003), Subdaily sea ice motion and deformation from RADARSAT observations, *Geophys. Res. Lett.*, **30**(23), 2218, doi:10.1029/2003GL018723.
- Kwok, R., G. F. Cunningham, and S. S. Pang (2004), Fram Strait sea ice outflow, *J. Geophys. Res.*, **109**, C01009, doi:10.1029/2003JC001785.
- Lindsay, R. W., and H. L. Stern (2003), The RADARSAT geophysical processor system: Quality of sea ice trajectory and deformation estimates, *J. Atmos. Oceanic Technol.*, **20**, 1333–1347, doi:10.1175/1520-0426[2003]020<1333:TRGPSQ>2.0.CO;2.
- Maslanik, J. A. (1992), Effects of weather on the retrieval of sea ice concentration and ice type from passive microwave data, *Int. J. Remote Sens.*, **13**(1), 37–54, doi:10.1080/01431169208904024.
- Proshutinsky, A. Y., and M. A. Johnson (1997), Two circulation regimes of the wind-driven Arctic Ocean, *J. Geophys. Res.*, **102**(C6), 12,493–12,514, doi:10.1029/97JC00738.
- Rasmussen, E. A., P. S. Guest, and K. L. Davidson (1997), Synoptic and mesoscale atmospheric features over the ice-covered portion of the Fram Strait in spring, *J. Geophys. Res.*, **102**(D12), 13,975–13,986, doi:10.1029/96JD03361.
- Schröder, D. (2005), Wirkung von Zyklonen auf das Meereis in der Framstraße: Modellrechnungen und Beobachtungen, 147 pp., Ph.D. thesis, Dep. of Geosci., Univ. of Hamburg, Hamburg, Germany.
- Spreen, G., L. Kaleschke, and G. Heygster (2008), Sea ice remote sensing using AMSR-E 89-GHz channels, *J. Geophys. Res.*, **113**, C02S03, doi:10.1029/2005JC003384.
- Svendsen, E., C. Mätzler, and T. C. Grenfell (1987), A model for retrieving total sea ice concentration from a spaceborne dual-polarized passive mi-

- crowave instrument operating near 90 GHz, *Int. J. Remote Sens.*, 8(10), 1479–1487, doi:10.1080/01431168708954790.
- Vinje, T. (2001), Fram Strait ice fluxes and atmospheric circulation: 1950–2000, *J. Clim.*, 14, 3508–3517, doi:10.1175/1520-0442[2001]014<3508:FSIFAA>2.0.CO;2.
- Vinje, T. and Ø. Finnekåsa (1986), The ice transport through Fram Strait, *Rep. 186*, 39 pp., Norsk Polarinst., Oslo.
- J. Launiainen, Finnish Institute of Marine Research, Erik Palmenin Aukio 1, PL 2, FIN-00561 Helsinki, Finland.
- D. Schröder, Department of Environmental Meteorology, University of Trier, Behringstrasse 21, Campus II, D-54286 Trier, Germany.
- G. Spreen, Institute of Oceanography, University of Hamburg, Bundesstrasse 53, D-20146 Hamburg, Germany.

B. Brümmner, A. Jahnke-Bornemann, and G. Müller, Meteorological Institute, University of Hamburg, Bundesstrasse 55, D-20146 Hamburg, Germany. (burghard.bruemmer@zmaw.de)